Graphical Table of Contents

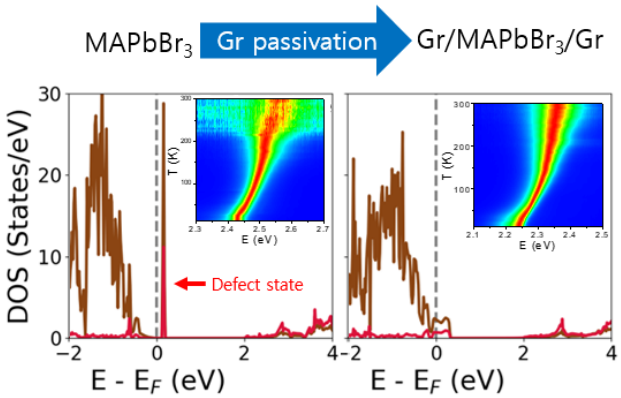

Summary

Controlling or passivating the surface defects in perovskite materials is a key parameter to enhance the high photoluminescence quantum efficiency. An enhanced quantum efficiency for perovskite $MAPbBr_3$ (MA = methylammonium) nanocrystals was demonstrated by encapsulating the $MAPbBr_3$ with graphene (Gr) arising from defect passivation, a conclusion supported by density functional theory calculations.

Enhanced photoluminescence quantum yield of $MAPbBr_3$ nanocrystals by passivation using graphene

Youngsin Park[1], Atanu Jana[1], Chang Woo Myung[1], Taeseung Yoon[1], Geunsik Lee[1], Claudius C. Kocher[2], Guanhua Ying[2], Vitaly Osokin[2], Robert A. Taylor[2] (✉), Kwang S. Kim[1] (✉)

[1]*School of Natural Science, Ulsan National Institute of Science and Technology, Ulsan 44919, Korea*

[2]*Clarendon Laboratory, Department of Physics, University of Oxford, Parks Road, Oxford OX1 3PU, UK*

Address corresponding to Robert A. Taylor, robert.taylor@physics.ox.ac.uk; Kwang S. Kim, kimks@unist.ac.kr

ABSTRACT

Diminishing surface defect states in perovskite nanocrystals is a highly challenging subject for enhancing optoelectronic device performance. We synthesized organic/inorganic lead-halide perovskite $MAPbBr_3$ (MA = methylammonium) clusters comprising nanocrystals with diameters ranging between 20~30 nm and characterized an enhanced photoluminescence (PL) quantum yield (as much as ~7 times) by encapsulating the $MAPbBr_3$ with graphene (Gr). The optical properties of $MAPbBr_3$ and Gr/ $MAPbBr_3$ were investigated by temperature-dependent micro-PL and time-resolved PL measurements. Density functional theory calculations show that the surface defect states in $MAPbBr_3$ are removed and the optical band gap is reduced by an 0.15 eV by encapsulation with graphene due to partial restoration of lattice distortions.

KEYWORDS

perovskite, nanoclusters, photoluminescence, surface passivation, graphene, density functional theory calculations.

1 Introduction

Given their low cost, high power conversion solar cell efficiency and high luminescence efficiency, light emitting diodes (LEDs), and organic/inorganic hybrid lead-halide perovskites $MAPbX_3$ (MA = CH_3NH_3, methylammonium, and X = Cl, Br, I) have been studied extensively [1-9]. In addition, the band gap of these hybrid lead-halide perovskites can be tuned over the whole visible region by halide substitutions and by the ratio of A-site cations [10-13]. In particular, the bromide perovskite ($MAPbBr_3$) has been studied widely due to its large band gap change and the stability [14]. Theoretically, the optical band gap of the $MAPbBr_3$ is calculated to be 2.2~2.3 eV [15]. In addition, experimentally it is found to depend upon the crystal type, that is, the gap is ~2.246 eV for single crystals [16], ~2.15 eV for thin films [17], ~2.214 eV for microcuboids [18], ~2.204 eV for microstructures [19] and ~2.36 eV for quantum dots (QDs) [20] due to quantum confinement effects. High photoluminescence quantum yield (PLQY) is only seen when high excitation powers or high current densities are employed, due to the presence of defects in $MAPbBr_3$ causing nonradiative process [21]. Surface defects need to be passivated properly on the $MAPbBr_3$ surface to achieve a high PLQY [22]. In semiconductor materials, the electric and optical properties can be modified by controlling the intrinsic defects [23]. Surface defects become more dominant in nanoscale materials given the increasing surface to volume ratio. A giant enhancement in the PL of $CsPbCl_3$ perovskite NCs was reported by dual-surface passivation [24], Lewis base passivation [22], and surface passivation with a graphene oxide interlayer, which enhances the efficiency of perovskite solar cells [25]. If we are able to control or passivate the surface defects in organic-inorganic hybrid lead-halide perovskite materials, the desired high PLQY can be achieved.

Here, we show that the PL efficiency of the $MAPbBr_3$ nanocrystals is much enhanced when compared to pristine nanocrystals by encapsulating the $MAPbBr_3$ clusters (comprising

many nanocrystals with diameters 20~30 nm) using graphene (Gr/$MAPbBr_3$). The nanocrystals are sandwiched at the top and bottom by graphene sheets synthesized using chemical vapour deposition [26-28], as in our previous work where we encapsulated molecules with a graphene sheet [29]. The integrated PL intensity of pristine $MAPbBr_3$ reduces by two orders of magnitude as the nanocrystals warm from 10 K to 300 K, whereas that of Gr/$MAPbBr_3$/Gr reduces by only a factor of two, indicating that the PL quantum yield of Gr/$MAPbBr_3$/Gr is much enhanced (by about 7 times) when compared to that of pristine $MAPbBr_3$. The origin of the PL of $MAPbBr_3$ and Gr/$MAPbBr_3$ clusters is analysed by using temperature-dependent micro PL (μPL) and time-resolved PL (TRPL) techniques.

2 Experimental

2.1 Sample preparation

$PbBr_2$ (98%), HBr (48% in water), γ-butyrolactone (99%) and N, N-dimethylformamide (DMF) were purchased from Sigma-Aldrich. Methylamine (40% in methanol) was purchased from Tokyo Chemical Industry (TCI). Octylammonium bromide and methylammonium bromide were prepared according to a method described previously [30]. Octylammonium bromide (25.2 mg, 0.12 mmol), methylammonium bromide 8.8 mg, 0.08 mmol) and $PbBr_2$ (73.4 mg, 0.2 mmol) were dissolved in 1 ml DMF. This homogeneous mixture was added to 4 mL γ- butyrolactone while being stirred at room temperature, which continued for 10 min. The addition of 15 mL of ether immediately produced a greenish yellow colloidal solution which was centrifuged at 5000 rpm for 5 minutes. The yellow precipitate was redispersed in toluene for further characterization.

The graphene, prepared on a Cu foil, was transferred onto SiO_2 (300 nm)/Si by a poly (methylmethacrylate) (PMMA)-assisted wet-transfer method. The PMMA was spin coated onto Gr/Cu foil. The PMMA-coated Gr was placed in a solution of Cu etchant (CE-100,

Transene Company, Inc.) to remove the Cu foil. After the Cu foil was completely removed away, the PMMA-coated Gr was scooped using the Au patterned SiO_2. The PMMA layer was then removed with acetone, and the sample was rinsed several times with DI water. The $MAPbBr_3$ nanocrystals were put in a toluene solution and the solution was treated under sonication for 10 min. Then the solution was dispersed on the desired substrate. In order to compensate for surface defects, we also prepared $MAPbBr_3$ clusters encapsulated with graphene (Gr/$MAPbBr_3$). A graphene layer was transferred onto the Au patterned SiO_2 substrate prior to the dispersion of the $MAPbBr_3$ solution. Finally, a second graphene layer was transferred onto the substrate to encapsulate the $MAPbBr_3$ clusters.

2.2 Transmission Electron Microscopy and X-ray Diffraction

Transmission electron microscopy images were taken on a JEOL JEM-2100F electron microscope using a 200 kV electron source. Samples were prepared on 200-mesh carbon coated Cu grids by dropping NC solutions that allowed for evaporation (see Fig. S1.) The powder X-ray diffraction was done on a D/MAX2500V/PC diffractometer, Rigaku using Cu-rotating anode X-rays. The Bragg diffraction angle (2θ) range was set to 10-50° and scan rate was 2°/ minute (see Fig. S2).

2.3 Photoluminescence and time-resolved photoluminescence

A frequency-doubled Ti:sapphire laser operating at 400 nm with a pulse-picked repetition rate of 50 kHz was used to excite the $MAPbBr_3$ in the μ-PL experiments. The incident laser power on the $MAPbBr_3$ surface was 20 nW. The sample was mounted in a continuous-flow helium cryostat, allowing the temperature to be controlled accurately from 10 K to room temperature. PL measurements were taken in increments of 5 K. A 100× objective was held by a sub-micron precision piezoelectric stage above the cryostat and used to focus the incident laser beam to a spot size of ~1 μm^2 and to collect the resulting luminescence. The luminescence was then directed to a spectrometer with a spectral resolution of ~700 μeV. The signal was

finally detected using a cooled charge coupled device (CCD) detector. All the PL spectra were obtained by using a 0.3 m focal length spectrometer with a 300 gr/mm grating. Time resolved photoluminescence (TRPL) measurements were carried out using the same experimental set up as above. The dispersed PL was reflected towards a photomultiplier connected to a commercial photon counting system (Becker&Hickl SPC-130), with a time resolution of ~130 ps. Measurements of the lifetimes of the confined states were then carried out over a range of excitation power densities.

2.4 DFT Calculations

Density functional theory (DFT) calculations were performed using the Vienna Ab initio Simulation Package (VASP) [31] with the PBE functional [32] plus Takatchenko-Scheffler van der Waals correction [33] including dipole corrections in conjunction with projector-augmented plane-wave basis set of 500 eV energy cut-off. The hexagonal $MAPbBr_3$ slab was constructed from the cubic $MAPbBr_3$ with the lattice mismatch of ~2 % to graphene and *k*-points were sampled with a Γ-centered (4 x 2 x 1) mesh. The charge analysis was conducted using Bader charge analysis code version 1.03 [34].

3 Results and discussion

The $MAPbBr_3$ clusters with average lateral diameters ~2 to ~7 μm are dispersed on an Au patterned SiO_2 substrate (Fig.1a). Fig. 1b shows the μPL spectra of the $MAPbBr_3$ with different cluster sizes taken at the positions in Fig.1a. The μPL energy depends strongly on the cluster size, which decreases rapidly from ~2.7 eV to ~2.45 eV as the cluster size increases from ~2.1 to ~4 μm the rate of change of the energy shift decreases, whilst the PL intensity increases, as shown in the inset. Although, in general, the PL emission energy depends on the size of the QDs, which is less than the Bohr radius of ~2 nm, we note that the PL emission

energy of $MAPbBr_3$ strongly depends on the size of the clusters which is similar to the energy dependence with crystal grain size seen by Chin *et al* [35]. The origin of this effect is still unclear, however one possible explanation is that energy transfer to a small proportion of larger nanoparticles is more likely in larger clusters, fostering a red shift in the emission, which would also explain why the shift gets smaller for the largest clusters, approaching the energy seen in single crystals ~ 2.3 eV, as the spread in nanoparticle size is finite. The overt energy difference between small and large clusters is more than > 0.3 eV which suggests a new pathway for bandgap tuning instead of the exchange of halides or the tuning of the A-site cation ratio. The temperature-dependent μPL measurements of the $MAPbBr_3$ clusters were carried out at the positions shown in Fig. 2a-c.

In order to elucidate the effect of graphene encapsulation on the $MAPbBr_3$ cluster, $MAPbBr_3$/Gr, and Gr/$MAPbBr_3$/Gr are also prepared on the Au patterned SiO_2 substrates (Fig. 2b and 2c). The graphene layer is clearly observed in the optical microscopy image and confirmed by measuring Raman spectra (see Fig. S3). Fig. 2d, 2e, and 2h show the temperature-dependent normalized PL spectral maps of the $MAPbBr_3$, $MAPbBr_3$/Gr, and Gr/$MAPbBr_3$/Gr clusters, respectively, at temperatures ranging from 10 to 300 K. It clearly shows that the PL emission energy shifts to high energy with increasing temperature and the samples also undergo phase transitions at certain marked temperatures. However, there are several big differences in the PL energy shifts between these samples. Firstly, we notice that the variation of the PL energy of the $MAPbBr_3$ cluster with temperature shows three kinks (lateral red arrows) near 25 K, 170 K, and ~260 K due to phase transitions of the hybrid lead-halide perovskite [24, 36, 37]. However, we do not observe these specific kinks in Gr/$MAPbBr_3$/Gr.

When the $MAPbBr_3$ is encapsulated with graphene, we expect that the abrupt lattice variation of $MAPbBr_3$ is mechanically protected because the thermal expansion coefficient of

graphene is negative [38, 39]. A similar effect was observed in $CsPbBr_xI_{3-x}$/PbS where stable PbS colloidal QDs protect the cubic phase of $CsPbBr_xI_{3-x}$ below the critical temperature by mechanically anchoring to $CsPbBr_xI_{3-x}$ [40]. Secondly, although we use $MAPbBr_3$ clusters of similar size for $MAPbBr_3$, $MAPbBr_3$/Gr, and Gr/$MAPbBr_3$/Gr samples, their PL emission energies are quite different. The PL energy of $MAPbBr_3$ is about ~2.43 eV (~510 nm), while that of $MAPbBr_3$/Gr, Gr/$MAPbBr_3$/Gr redshifts to ~2.34 eV (529.8 nm) and ~2.23 eV (~556 nm) at 10 K, the Gr can modify the band gap. This is well confirmed by DFT calculations (discussed later). Thirdly, while the full width at half maximum (FWHM) is almost constant below 100 K and then increases above 100 K for the $MAPbBr_3$ cluster, that of Gr/$MAPbBr_3$/Gr decreases with the increasing in temperature up to 100 K but then increases monotonically above 100 K.

In order to extract physical parameters such as emission energy, FWHM, and integrated PL intensity of the PL spectra as a function of temperature in the region from 10 to 300 K, all the spectra were paramaterised using a Voigt profile. Some typical spectra at several temperatures are shown in Fig. 3. The PL spectrum at 10 K shows an asymmetric shape, which may originate from an exciton-exciton scattering in the low temperature regime and surface defects due to large surface to volume ratio [20, 41]. This indicates the existence of more than two components at least. For the $MAPbBr_3$ cluster, the main emission energy is about 2.429 eV with a FWHM of ~37.3 meV (7.23 nm), and two emission lines are enough to reconstruct the PL spectrum with an additional shoulder peak centered at 2.398 eV (cyan line) which may originate from surface defects (Fig. 3a). While the PL peaks shift to high energy, the low energy PL peak almost disappears after ~80 K, and the main peak remains up to room temperature. As we expected, the intensity above 200 K is very low. However, the PL spectrum of Gr/$MAPbBr_3$/Gr is broader and more asymmetric than that of $MAPbBr_3$ at 10 K. The total FWHM of the Gr/$MAPbBr_3$ is about 50 meV (12 nm) and it can be reconstructed

by three peaks (Fig. 3b). In a similar manner to the 2.398 eV peak of $MAPbBr_3$, the lowest energy peak (cyan solid line) disappears rapidly above ~50 K due to the passivation of surface defects by the graphene encapsulation. An additional peak (green solid line) at 2.214 eV shifts to high energy and disappears above ~180 K. Though the origin of this peak is unclear, we can expect a new peak due to interface-defects because the $MAPbBr_3$ is mechanically contacted to graphene. This interface also causes strain because of the opposite thermal expansion coefficients for $MAPbBr_3$ and graphene. Finally, the main peak (blue solid line) positioned at ~2.24 eV remains above room temperature. Unlike pristine $MAPbBr_3$, the PL peak intensity at room temperature is not quenched, implying a high PLQY.

In order to characterize the PLQY in $MAPbBr_3$ and graphene encapsulated $MAPbBr_3$, we compare the integrated PL intensities over the whole temperature range. As shown in Fig. 3, the PL peak intensity of the $MAPbBr_3$ becomes very low and noisy above ~200 K, whereas that of graphene encapsulated $MAPbBr_3$ is still intense and clear. From the best fitting results, the integrated PL intensity is presented as a function of temperature (Fig. 4a and b). The integrated PL intensity ratio at low versus room temperature (I_{10K}/I_{300K}) changes from 38.1 for $MAPbBr_3$ to 5.14 for $Gr/MAPbBr_3/Gr$. From these results, we can conclude that the QY of the $Gr/MAPbBr_3/Gr$ is enhanced by ~7.4 times compared with that of the $MAPbBr_3$. If we assume that the quantum yield is 100% at low temperature (5K), it decreases to 1% quantum yield due to the decrease in the PL intensity of two orders of magnitude at room temperature [42].

The PL enhancement is related to an increased exciton binding energy or a reduction in the defect density. The thermal activation energy or exciton binding energy can be deduced by using the equation of $I(T) = I_0/(1 + A\exp(-E_b/k_B T)$, in which I_0 is the intensity at 0K, E_b is the exciton binding energy, and k_B is the Boltzmann constant. In order to determine the activation energy of the samples, the intensity variation as a function of temperature was fitted

by an Arrhenius function (see Fig. S4). The fitted binding energy for the $MAPbBr_3$ above ~100 K is ~86.6 meV, which is large compared to ~13 meV for a single crystal [16], ~53.3 meV for microstructures [19], ~54.8 meV for microcuboids [18], ~65 meV for bulk [20], and 76 meV for polycrystalline thin film [43]. Though the value is small compared with the binding energy of ~375 meV of $MAPbBr_3$ QDs [20], it is large enough to give excitonic emission at temperatures of a few hundred K. In addition, the binding energy for the Gr/$MAPbBr_3$/Gr increases to ~104.6 meV, contributing to the excellent PL efficiency at high temperature.

The PL peak broadening with temperature provides information on inhomogeneous features of the samples as well as on the coupling between excitons and phonons. Fig. 4c and d show the FWHM as a function of temperature. The FWHM of the main peak of $MAPbBr_3$ shows a small linear increase up to ~70 K, and then broadens more steeply as the temperature increases up to ~300 K where the FWHM of ~140 meV is slightly larger than that of a $MAPbBr_3$ thin film (~100 meV) [17]. For the graphene encapsulated $MAPbBr_3$, however, the FWHM decreases linearly up to ~100 K and then increases up to ~60 meV at 300 K, which is less than a half that for pristine $MAPbBr_3$. This behaviour at low temperatures is quite atypical. The thermal broadening of the emission linewidth due to the exciton-phonon interaction can be expressed by the following equation [44],

$$\Gamma(T) = \Gamma_0 + \sigma T + \gamma_{\mathrm{LO}}/[\exp\left(-\frac{E_{\mathrm{LO}}}{k_{\mathrm{B}}T}\right) - 1],$$

which is denoted as red solid lines in Fig 4c and d. Γ_0 in the first term represents the temperature-independent inhomogeneous broadening at $T = 0$ K.

The homogenous broadening due to exciton-phonon interactions can be deduced by the last two terms. Here, σ and γ_{LO} are the coupling coefficient between an exciton and an acoustic phonon and that between the exciton and the longitudinal optical (LO)

phonon, respectively. E_{LO} in the last term is the LO phonon energy. The values of E_{LO} for $MAPbBr_3$ and Gr/$MAPbBr_3$/Gr are calculated to be ~53.6 meV and 32.2 meV, respectively, indicating a strong exciton-phonon interaction. Though these values are 2~3 times larger than the value (15.3 meV) in $MAPbBr_3$ thin film [17], they are close to the value (42.2 meV) of $MAPbBr_3$ QDs [20] which is in good agreement with the unresolved Raman mode of ~340 cm^{-1} (42.2 meV) in $MAPbI_3$ [45]. Moreover, the position of MA molecule-related modes should be higher than 300 cm^{-1} [16].

Fig. 5a shows the TRPL decay curve of the $MAPbBr_3$ and Gr/$MAPbBr_3$/Gr measured at 10 K. The charge carrier kinetics can be modelled with following coupled differential equations to describe the decay dynamics of the organic-inorganic materials [46, 47].

$$-\frac{dn_f}{dt} = k_{f1}n_f + k_{f2}n_f^2 + k_{f3}n_f^3 \quad (1),$$

$$-\frac{dn_x}{dt} = k_x n_x \quad (2).$$

Eq. (1) has three contributions governed by three different drivers of recombination dynamics. The first term k_{f1} arises from trap-assisted recombination, k_{f2} is the free carrier recombination rate, and k_{f3} is the Auger recombination rate. At low temperatures excitonic decay [Eq. (2)] can also be significant. Here we assume the exciton density (n_x) and the free-carrier decay (n_f) are independent of each other. Only k_{f2} and k_x describe radiative recombination and all the other parameters are assumed non-radiative. These equations produce good fits to the data and the resultant fitted parameters are summarized in Table I.

The free carrier density of the $MAPbBr_3$ is much higher than that for Gr/$MAPbBr_3$/Gr because the free carriers filled trap states [48]. Conversely, the exciton density of the Gr/$MAPbBr_3$/Gr is about twice that of the $MAPbBr_3$ contributing to the observed radiative recombination rate. The trap-assisted recombination rate of the $MAPbBr_3$ is much higher than that of the Gr/$MAPbBr_3$/Gr. As the trap states in perovskites are intrinsic and increase with

temperature [49], we can speculate that it is due to thermally activated atomic vacancies [49-51]. These defects can be compensated by mechanical protection using graphene due to its negative thermal expansion coefficient.

Fig. 5b shows the TRPL decay trends of $MAPbBr_3$ and Gr/$MAPbBr_3$/Gr measured at 300 K. Though we observe only single peak PL spectra at a high temperature regime, the TRPL spectra are fitted well by using a bi-exponential decay model, where the fast component (τ_1) and slow component (τ_2) of the emission peak arise from different origins. The decay times of τ_1 and τ_2 are 4.9±0.14 ns and 20.1±1.1 ns, respectively, for the $MAPbBr_3$, are very similar to those seen for colloidal $MAPbBr_3$ QDs originating from the initial excitonic decay upon light absorption and exciton radiative recombination with surface states due to the stable excitons [20]. These decay times increase more in Gr/$MAPbBr_3$/Gr with the values of ~5.1±0.16 ns and 25.4±1.3 ns, respectively. The fast component is similar to that of $MAPbBr_3$, however, the slow component increases by ~5 ns, implying that the surface state is more stable due to reduced intrinsic defects arising from graphene passivation.

To better understand the graphene passivation mechanism, we performed DFT calculations [52] using the PBE+TS functional [53] with and without graphene on a $PbBr_2$-terminated Pb-vacant $MAPbBr_3$ surface. The distance between the graphene and the $MAPbBr_3$ is d = 3.43Å, indicating that graphene physisorbs to $MAPbBr_3$ without any chemical bonding. A charge transfer (CT) of 0.21e per unit-cell from graphene to the $MAPbBr_3$ slab occurs and most of the CT, 0.2e per unit-cell, is to the first PbI_2 surface layer. The geometry optimizations of two surfaces (Fig. 6a, b) reveal an explicit role for graphene acting on $MAPbBr_3$ surface defects. Without graphene encapsulation, we observe severe lattice distortions of the Br-Pb-Br frame ($\theta_{Br\text{-}Pb\text{-}Br}$ ~147.6°) compared to the case with graphene ($\theta_{Br\text{-}Pb\text{-}Br}$ ~168.9°). As expected, the Pb-vacancy of $MAPbBr_3$ forms only a shallow

level just above the valence band maximum from the density of states calculation (Fig. 6c) [54]. However, upon graphene encapsulation, followed by partial restoration of lattice distortions, the defect state is removed (Fig. 6d). The band gap of $MAPbBr_3$ after the graphene encapsulation decreases by 0.15 eV from the DFT calculation, which is consistent with the experimental observation of ~0.2 eV. Although studies on graphene encapsulation of the pristine surface of tetragonal $MAPbI_3$ or cubic $CsPbI_3$ have been carried out [55, 56], the role of graphene encapsulation on defect passivation of perovskite solar cell materials has not yet been realized.

4 Conclusion

In summary, we have characterized the enhanced photoluminescence quantum yield of organic-inorganic hybrid lead-halide perovskite $MAPbBr_3$ clusters comprised of nanocrystals with diameter 20~30 nm using μ-PL and time-resolved PL. Once the $MAPbBr_3$ clusters are encapsulated by graphene to passivate the surface defects on the $MAPbBr_3$, the PL efficiency is enhanced (as much as 7 times) over the $MAPbBr_3$ clusters. From the temperature-dependent PL measurements, the exciton binding energies are calculated to be ~86.6 meV for $MAPbBr_3$ and ~104.6 meV for the Gr/$MAPbBr_3$/Gr, causing the greatly improved PL efficiency at high temperatures. The FWHMs of the $MAPbBr_3$ and Gr/$MAPbBr_3$ clusters are deduced to be 53.6 meV and 32.2 meV, respectively, indicating strong exciton-phonon interaction. The decay time of Gr/$MAPbBr_3$/Gr is ~25 ns, 25 % longer than that of $MAPbBr_3$, implying that the surface state is more stabilized by the passivation of intrinsic defects. Density functional theory calculations support the experimental results that surface defect states in $MAPbBr_3$ are removed by graphene passivation causing a large enhancement in the PL efficiency due to partial restoration of lattice distortions.

Acknowledgements

Y.P., A.J., and C.W.M contributed equally to this work. This work was supported by Basic Science Research Program and National Honor Scientist Program through the National Research Foundation of Korea (NRF) (Grant Nos. 2010-0020414, 2015R1D1A1A01058332, 2018R1D1A1B07043676, 2019R1A4A1029237). K.S.K. acknowledges the support from KISTI (KSC-2018-CRE-0077, KSC-2018-CHA-0057). C.W.M. acknowledges the support from KISTI (KSC-2018-CRE-0071, KSC-2019-CRE-0139, KSC-2019-CRE-0248).

Electronic Supplementary Material: Supplementary material (TEM images, XRD, and Raman spectroscopy data) is available in the online version of this article at https:// //dx.doi.org/10.1007/*********.

References

[1] Park, N.; Grätzel, M.; Miyasaka, T.; Zhu, K.; Emery, K. Towards stable and commercially available perovskite solar cells. *Nat. Energy* **2016**, *1*, 16152.

[2] deQuilettes, D. W.; Vorpahl, S. M.; Stranks, S. D.; Nagaoka, H.; Eperon, G. E.; Ziffer, M. E.; Snaith, H. J.; Ginger, D. S. Impact of microstructure on local carrier lifetime in perovskite solar cells. *Science* **2015**, *348*, 683–686.

[3] Yang, W. S.; Park, B.-W.; Jung, E. H.; Jeon, N. J.; Kim, Y. C.; Lee, D. U.; Shin, S. S.; Seo, J.; Kim, E. K.; Noh, J. H.; Seok, S. I. Iodide management in formamidinium-lead-halide−based perovskite layers for efficient solar cells. *Science* **2017**, 356, 1376-1379.

[4] Luo, J.; Im, J.-H.; Mayer, M. T.; Schreier, M.; Nazeeruddin, M. K.; Park, N.-G.; Tilley, S. D.; Fan, H. J.; Grätzel, M. Water photolysis at 12.3% efficiency via perovskite photovoltaics and earth-abundant catalysts. *Science* **2015**, *345*, 1593–1597.

[5] Manser, J. S.; Kamat, P. V. Band filling with free charge carriers in organometal halide perovskites. *Nat. Photonics* **2014**, *8* (9), 737–743.

[6] Myung, C. W.; Yun, J.; Lee, G.; Kim, K. S. A new perspective on the role of A-site cations in perovskite solar cells, *Adv. Energy Mater.* **2018**, *8*, 1702898.

[7] Jana, A.; Kim, K. S. Water-stable, fluorescent organic−inorganic hybrid and fully inorganic perovskites, *ACS Energy Lett.* **2018**, *3*, 2120-2126.

[8] Cho, H.; Jeong, S.-H.; Park, M.-H.; Kim, Y.-H.; Wolf C.; Lee, C.-L.; Heo, J. H.; Sadhanala, A.; Myoung, N.; Yoo, S.; Im, S. H.; Friend, R. H.; Lee, T.-W. Overcoming the electroluminescence efficiency limitations of perovskite light-emitting diodes. *Science* **2015**, 350, 1222-1225.

[9] Seo, H.-K.; Kim, H.; Lee, J.; Park, M.-H.; Jeong, S.-H.; Kim, Y.-H.; Kwon, S.-J.; Han, T.-H.; Yoo, S.; Lee, T.-W. Efficient flexible organic/inorganic hybrid perovskite light-emitting diodes based on graphene anode. *Adv. Mater*. **2017**, 29, 1605587-000000.

[10] Tombe, S.; Adam, G.; Heilbrunner, H.; Apaydin, D. H.; Ulbricht, C.; Sariciftci, N. S.; Arendse, C. J.; Iwuoha, E.; Scharber, M. C. Optical and electronic properties of mixed halide (X = I, Cl, Br) methylammonium lead perovskite solar cells. *J. Mater. Chem. C* **2017**, *5*, 1714–1723.

[11] Cui, D.; Yang, Z.; Yang, D.; Ren, X.; Liu, Y.; Wei, Q.; Fan, H.; Zeng, J.; Liu, S. Color-tuned perovskite films prepared for efficient solar cell applications. *J. Phys. Chem. C* **2016**, *120*, 42–47.

[12] Kulkarni, S. A.; Baikie, T.; Boix, P. P.; Yantara, N.; Mathews, N.; Mhaisalkar, S. Band-gap tuning of lead halide perovskites using a sequential deposition process. *J. Mater. Chem. A* **2014**, *2*, 9221–9225.

[13] Mittal, M.; Jana, A.; Sarkar, S.; Mahadevan, P.; Sapra, S. Size of the organic cation tunes the band gap of colloidal organolead bromide perovskite nanocrystals. *J. Phys. Chem. Lett.* **2016**, *7*, 3270–3277.

[14] Yang, Y.; Yan, Y.; Yang, M.; Choi, S.; Zhu, K.; Luther, J. M.; Beard, M. C. Low surface recombination velocity in solution-grown $CH_3NH_3PbBr_3$ perovskite single crystal. *Nat. Commun.* **2015**, *6*, 7961.

[15] Shi, T.; Yin, W. J.; Hong, F.; Zhu, K.; Yan, Y. Unipolar self-doping behavior in perovskite $CH_3NH_3PbBr_3$. *Appl. Phys. Lett.* **2015**, *106*, 103902.

[16] Lozhkina, O. A.; Yudin, V. I.; Murashkina, A. A.; Shilovskikh, V. V.; Davydov, V. G.; Kevorkyants, R.; Emeline, A. V.; Kapitonov, Y. V.; Bahnemann, D. W. Low inhomogeneous broadening of excitonic resonance in $MAPbBr_3$ single crystals. *J. Phys. Chem. Lett.* **2018**, *9*, 302–305.

[17] Wright, A. D.; Verdi, C.; Milot, R. L.; Eperon, G. E.; Pérez-Osorio, M. A.; Snaith, H. J.; Giustino, F.; Johnston, M. B.; Herz, L. M. Electron–phonon coupling in hybrid lead halide perovskites. *Nat. Comm*. **2016**, *7*, 11755.

[18] Chen, F.; Zhu, C.; Xu, C.; Fan, P.; Qin, F.; Gowri Manohari, A.; Lu, J.; Shi, Z.; Xu, Q.; Pan, A. Crystal structure and electron transition underlying photoluminescence of methylammonium lead bromide perovskites. *J. Mater. Chem. C* **2017**, *5*, 7739–7745.

[19] Dai, J.; Zheng, H.; Zhu, C.; Lu, J.; Xu, C. Comparative investigation on temperature dependent photoluminescence of $CH_3NH_3PbBr_3$ and $CH(NH_2)_2PbBr_3$ microstructures. *J. Mater. Chem. C* **2016**, *4*, 4408–4413.

[20] Zhang, F.; Zhong, H.; Chen, C.; Wu, X. G.; Hu, X.; Huang, H.; Han, J.; Zou, B.; Dong, Y. Brightly luminescent and color-tunable colloidal $CH_3NH_3PbX_3$ (X = Br, I, Cl) quantum dots: potential alternatives for display technology. *ACS Nano* **2015**, *9*, 4533–4542.

[21] Deschler, F.; Price, M.; Pathak, S.; Klintberg, L. E.; Jarausch, D. D.; Higler, R.; Hüttner, S.; Leijtens, T.; Stranks, S. D.; Snaith, H. J.; Atatüre, M.; Phillips, R. T.; Friend, R. H. High photoluminescence efficiency and optically pumped lasing in solution-processed mixed halide perovskite semiconductors. *J. Phys. Chem. Lett.* **2014**, *5*, 1421–1426.

[22] Noel, N. K.; Abate, A.; Stranks, S. D.; Parrott, E. S.; Burlakov, V. M.; Goriely, A.; Snaith, H. J. Enhanced photoluminescence and solar cell performance via Lewis base passivation of organic-inorganic lead halide perovskites. *ACS Nano* **2014**, *8*, 9815–9821.

[23] Queisser, H. J.; Haller, E. E. Defects in semiconductors: some fatal, some vital *Science* **1998**, *281*, 945–950.

[24] Ahmed, G. H.; El-Demellawi, J. K.; Yin, J.; Pan, J.; Velusamy, D. B.; Hedhili, M. N.; Alarousu, E.; Bakr, O. M.; Alshareef, H. N.; Mohammed, O. F. Giant photoluminescence enhancement in $CsPbCl_3$ perovskite nanocrystals by simultaneous dual-surface passivation. *ACS Energy Lett.* **2018**, *3*, 2301–2307.

[25] Li, H.; Tao, L.; Huang, F.; Sun, Q.; Zhao, X.; Han, J.; Shen, Y.; Wang, M. Enhancing efficiency of perovskite solar cells via surface passivation with graphene oxide interlayer. *ACS Appl. Mater & Inter.* **2017**, *9*, 38967−38976.

[26] Kim, K. S.; Zhao, Y.; Jang, H.; Lee, S. Y.: Kim, J. M.; Kim, K. S.; Ahn, J.-H.; Kim, P.; Choi, J.-Y.; Hong, B. H., Large-scale pattern growth of graphene films for stretchable transparent electrodes. *Nature* **2009**, *457*, 706-710.

[27] Li, X.; Cai, W.; An, J.; Kim, S.; Nah, J.; Yang, D.; Piner, R.; Velamakanni, A.; Jung, I.; Tutuc, E.; Banerjee, S. K.; Colombo, L.; Ruoff, R. S. Large-area synthesis of high-quality and uniform graphene films on copper foils. *Scienc*e **2009**, *324*, 1312-1314.

[28] Bae, S.; Kim, H.; Lee, Y.; Xu, X.; Park, J.-S.; Zheng, Y.; Balakrishnan, J.; Lei, T.; Kim, H. R.; Song, Y. I.; Kim, Y.-J.; Kim, K. S.; Ozyilmaz, B.; Ahn, J.-H.; Hong, B. H.; Iijima, S. Roll-to-roll production of 30-inch graphene films for transparent electrodes. *Nat. Nanotech.* **2010**, *5,* 574-578.

[29] Yu, S. U.; Lee, H.; Cho, W. J.; Kim, C.; Kang, M. C.; Shin, H.-J.; Kim, N.; Hahn, S. K.; Kim, K. S. Spectromicroscopic observation of a live single cell in a biocompatible liquid-enclosing graphene system. *Nanoscale*, **2018**, *10*, 150-157.

[30] Teunis, M. B.; Jana, A.; Dutta, P.; Johnson, M. A.; Mandal, M.; Muhoberac, B. B.; Sardar, R. Mesoscale growth and assembly of bright luminescent organolead halide perovskite quantum wires. *Chem. Mater.* **2016**, *28*, 5043−5054.

[31] Kresse, G.; Furthmu, J. Efficient Iterative Schemes for *ab initio* Total-energy calculations using a plane-wave basis set. *Phys. Rev. B* **1996**, *54*, 11169.

[32] Perdew, J. P.; Burke, K.; Ernzerhof, M. Generalized gradient approximation made simple. *Phys. Rev. Lett.* **1996**, *77*, 3865–3868.

[33] Tkatchenko, A.; Distasio, R. A.; Car, R.; Scheffler, M. Accurate and efficient method for many-body van der Waals interactions. *Phys. Rev. Lett.* **2012**, *108*, 236402.

[34] Yu, M.; Trinkle, D. R. Accurate and efficient algorithm for bader charge integration. *J. Chem. Phys.* **2011**, *134*, 064111.

[35] Chin, S.-H.; Choi, J. W.; Woo, H. C.; Kim, J. H.; Lee, H. S.; Lee, C.-L. Realizing a highly luminescent perovskite thin film by controlling the grain size and crystallinity through solvent vapour annealing. *Nanoscale* **2019**, *11*, 5861-5867.

[36] Fang, H.-H.; Wang, F.; Adjokatse, S.; Zhao, N.; Even, J.; Antonietta Loi, M. Photoexcitation dynamics in solution-processed formamidinium lead iodide perovskite thin films for solar cell applications. *Light Sci. Appl.* **2015**, *5*, e16056.

[37] Onoda-Yamamuro, N.; Matsuo, T.; Suga, H. Calorimetric and IR spectroscopic studies of phase transtions in methylammonium trihalogenoplumabtes (II). *J. Phys. Chem. Solids* **1990**, *51*, 1383–1395.

[38] Zakharchenko, K. V.; Katsnelson, M. I.; Fasolino, A. finite temperature lattice properties of graphene beyond the quasiharmonic approximation. *Phys. Rev. Lett.* **2009**, *102*, 046808.

[39] Yoon, D.; Son, Y.-W.; Cheong, H. Negative thermal expansion coefficient of graphene measured by Raman spectroscopy. *Nano Lett.* **2011**, *11*, 3227–3231.

[40] Liu, M.; Chen, Y.; Tan, C.-S.; Quintero-Bermudez, R.; Proppe, A. H.; Munir, R.; Tan, H.; Voznyy, O.; Scheffel, B.; Walters, G.; Kam, A. P. T.; Sun, B.; Choi, M.-J.; Hoogland, S.; Amassian, A.; Kelley, S. O.; de Arquer, F. P. G.; Sargent, E. H. Lattice anchoring stabilizes solution-processed semiconductors. *Nature* **2019**, *570*, 96-101.

[41] Kunugita, H.; Kiyota, Y.; Udagawa, Y.; Takeoka,Y.; Nakamura, Y.; Sano, J.; Matsushita, T.; Kondo, T.; Ema, K. Exciton–exciton scattering in perovskite $CH_3NH_3PbBr_3$ single crystal. *Jpn. J. Appl. Phys*. **2016**, *55*, 060304.

[42] Fang, H.-H.; Raissa, R.; Abdu-Aguye, M.; Adjokatse, S.; Blake, G. R.; Even, J.; Loi, M. A. Photophysics of organic–inorganic hybrid lead iodide perovskite single crystals. *Adv. Funct. Mat.* **2015**, *25*, 2378–2385.

[43] Tanaka, K.; Takahashi, T.; Ban, T.; Kondo, T.; Uchida, K.; Miura, N. Comparative study on the excitons in lead-halide-based perovskitetype crystals $CH_3NH_3PbBr_3$ $CH_3NH_3PbI_3$. *Solid State Comm.* **2003**, *127*, 619–623

[44] Seguin, R.; Rodt, S.; Strittmatter, A.; Reißmann, L.; Bartel, T.; Hoffmann, A.; Bimberg, D.; Hahn, E.; Gerthsen, D. Multi-excitonic complexes in single InGaN quantum dots. *Appl. Phys. Lett.* **2004**, *84*, 4023–4025.

[45] Quarti, C.; Grancini, G.; Mosconi, E.; Bruno, P.; Ball, J. M.; Lee, M. M.; Snaith, H. J.; Petrozza, A.; Angelis, F. De. The Raman spectrum of the $CH_3NH_3PbI_3$ hybrid perovskite: interplay of theory and experiment. *J. Phys. Chem. Lett.* **2014**, *5*, 279–284.

[46] Wehrenfennig, C.; Eperon, G. E.; Johnston, M. B.; Snaith, H. J.; Herz, L. M. High charge carrier mobilities and lifetimes in organolead trihalide perovskites. *Adv. Mat.* **2014**, *26*, 1584–1589.

[47] Xing, G.; Wu, B.; Wu, X.; Li, M.; Du, B.; Wei, Q.; Guo, J.; Yeow, E. K. L.; Sum, T. C.; Huang, W. Transcending the slow bimolecular recombination in lead-halide perovskites for electroluminescence. *Nat. Comm.* **2017**, *8*, 14558.

[48] Stranks, S. D.; Burlakov, V. M.; Leijtens, T.; Ball, J. M.; Goriely, A.; Snaith, H. J. Recombination kinetics in organic-inorganic perovskites: excitons, free charge, and subgap states. *Phys. Rev. Appl.* **2014**, *2*, 034007.

[49] Smyth, D. M. Defect and order in perovskite-related oxides. *Annu. Rev. Mater. Sci.* **1985**, *15*, 329-357.

[50] Yin, W.-J.; Shi, T.; Yan, Y. Unusual defect physics in $CH_3NH_3PbI_3$ perovskite solar cell absorber. *Appl. Phys. Lett.* **2014**, *104*, 063903.

[51] Shkrob, I. A.; Marin, T. W. Charge trapping in photovoltaically active perovskites and related halogenoplumbate compounds. *J. Phys. Chem. Lett.* **2014**, *5*, 1066-1071.

[52] Kresse, G.; Furthmuller, J. Efficiency of Ab-Initio total energy calculations for metals and semiconductors using a plane-wave basis set. *Comput. Mater. Sci.* **1996**, *6*, 15−50.

[53] Tkatchenko, A.; Scheffler, M. Accurate molecular van Der Waals interactions from ground-state electron density and free-atom reference data. *Phys. Rev. Lett.* **2009**, *102* (7), 6–9.

[54] Huang, H.; Bodnarchuk, M. I.; Kershaw, S. V.; Kovalenko, M. V.; Rogach, A. L. Lead halide perovskite nanocrystals in the research spotlight: stability and defect tolerance. *ACS Energy Lett.* **2017**, *2*, 2071–2083.

[55] Volonakis, G.; Giustino, F. Ferroelectric graphene–perovskite interfaces. *J. Phys. Chem. Lett.* **2015**, *6*,2496–2502.

[56] Myung, C. W.; Javaid, S.; Kim, K. S.; Lee, G. Rashba-dresselhaus effect in inorganic/organic lead iodide perovskite interfaces. *ACS Energy Lett.* **2018**, *3*, 1294–1300.

Table 1 Fitting parameters from the TRPL traces measured at 10 K.

	free carrier density (cm^{-3})	exciton density (cm^{-3})	k_{f1} (s^{-1})	k_{f2} (cm^3s^{-1})
$MAPbBr_3$	4.6×10^{17}	1.5×10^{15}	3.2×10^{6}	1.98×10^{-13}
$Gr/MAPbBr_3$	0.4×10^{17}	2.4×10^{15}	2.0×10^{3}	2.84×10^{-11}

Figure captions

Figure 1 Optical microscopy and PL emission. (a) Optical microscopy image of the $MAPbBr_3$ clusters dispersed on an Au patterned SiO_2 substrate. The size was estimated along the lateral direction. (b) μPL spectra of the $MAPbBr_3$ nanoparticles with different cluster sizes. Inset depicts the PL energy and intensity as a function of $MAPbBr_3$ cluster size. Each color spectrum corresponds to the same colored circle marked in (a).

Figure 2 Optical microscopy and PL emissions. Optical microscopy images of $MAPbBr_3$ clusters dispersed on SiO_2 substrates (a) without graphene, (b) $MAPbBr_3$/Gr, and (c) Gr/$MAPbBr_3$/Gr. Normalized temperature-dependent PL maps of the $MAPbBr_3$ (d), $MAPbBr_3$/Gr (e) and Gr/$MAPbBr_3$/Gr (f).

Figure 3 Photoluminescence spectra**.** Temperature-dependent PL spectra of $MAPbBr_3$ (a) and Gr/$MAPbBr_3$/Gr (b). All spectra are reconstructed by fitting using a Voight profile. Solid circles are the measured data. The cyan, green and blue solid lines are the reconstructed peaks and red solid lines are the sum of the reconstructed peaks.

Figure 4 Photoluminescence intensity and FWHM. The integrated PL intensities of $MAPbBr_3$ (a) and Gr/$MAPbBr_3$/Gr (b). Circles are data obtained by fitting. The variation of the FWHM for the main PL peaks of $MAPbBr_3$ (c) and Gr/$MAPbBr_3$/Gr (d) are plotted as a function of temperature. Circles are the measured data and the red solid lines are the fitted results.

Figure 5 Time-resolved photoluminescence. (a), TRPL trace of the $MAPbBr_3$ (black circles) and Gr/$MAPbBr_3$/Gr (red circles) measured at 10 K. The black and red solid lines are fitted by coupled differential equations. (b), TRPL spectra of the $MAPbBr_3$ (black circles) and Gr/$MAPbBr_3$/Gr (red circles) measured at 300 K. The black and red solid lines are fitted by a biexponential decay function.

Figure 6. Density functional theory calculations. The geometry of a $PbBr_2$-terminated Pb-vacant $MAPbBr_3$ surface (a) without and (b) with graphene with Pb(red), Br(brown), C(grey), N(blue), and H(white) atoms. The density of states (DOS) of the $PbBr_2$-terminated Pb-vacant $MAPbBr_3$ surface (c) without and (d) with graphene. The DOS of surface Pb (red) and Br (brown) states clearly indicates the effect of defect passivation by graphene.

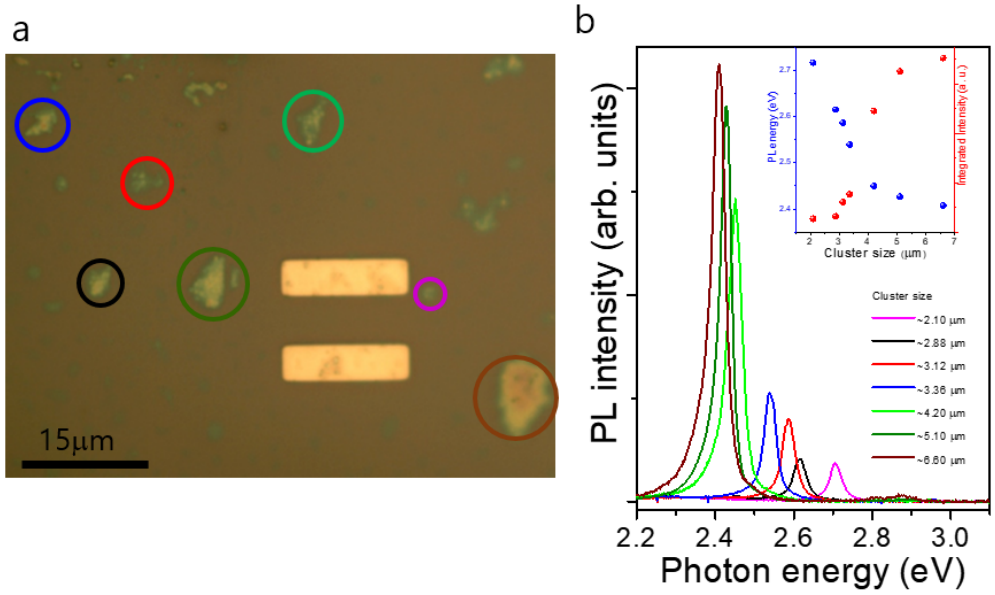
a
15μm
b
PL intensity (arb. units)
Photon energy (eV)
PL energy (eV)
Integrated Intensity (a. u.)
Cluster size (μm)
Cluster size
~2.10 μm
~2.88 μm
~3.12 μm
~3.36 μm
~4.20 μm
~5.10 μm
~6.60 μm

Fig. 1.

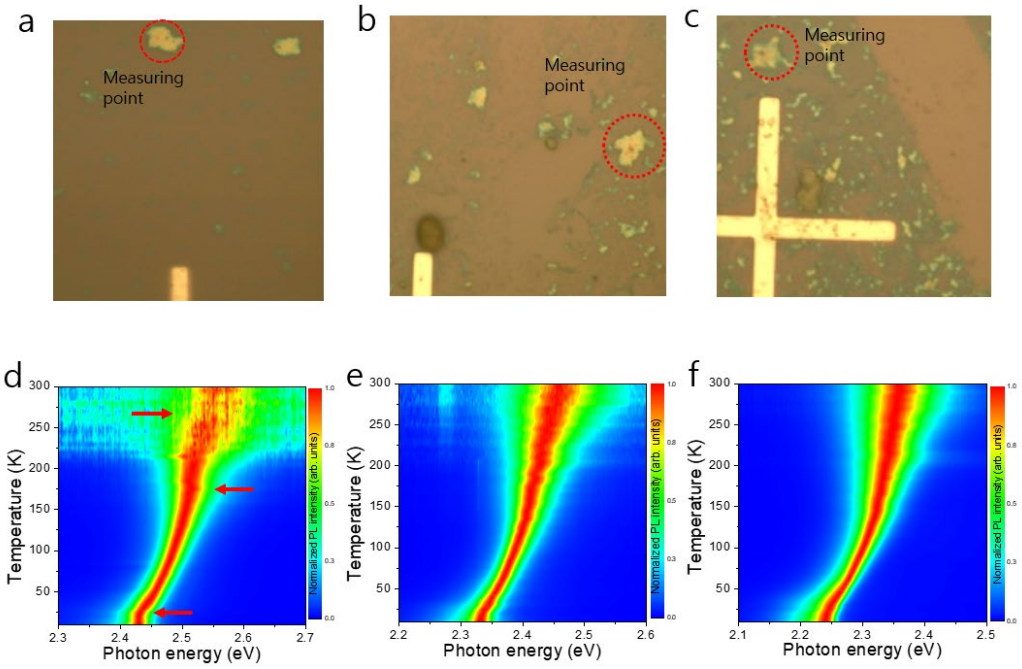
a
Measuring point
b
Measuring point
c
Measuring point
d
e
f
Temperature (K)
Photon energy (eV)
Normalized PL intensity (arb. units)

Fig. 2

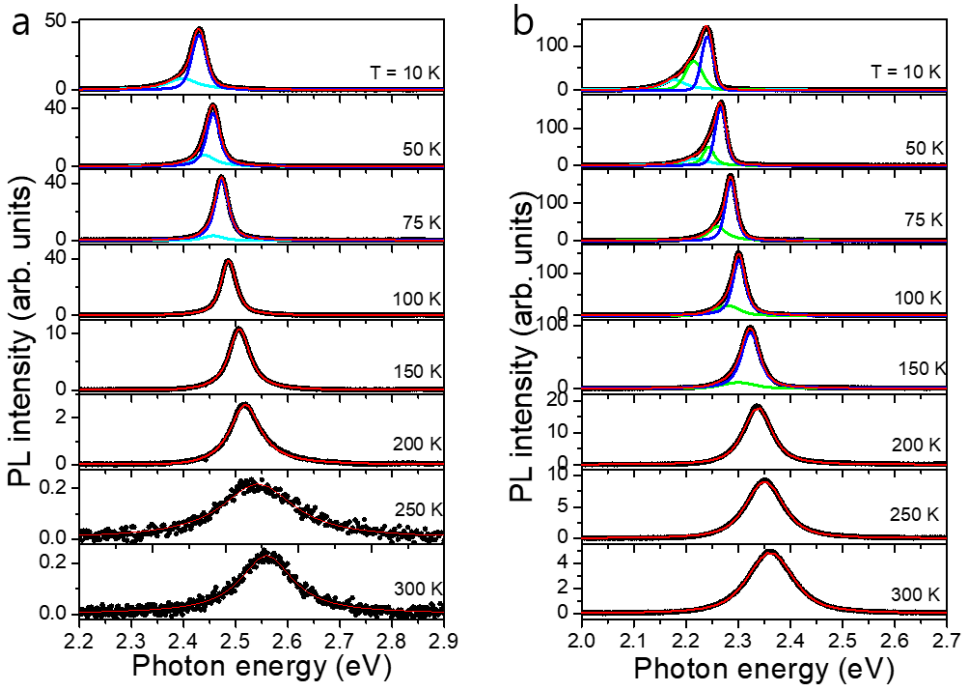
a
b
T = 10 K
50 K
75 K
100 K
150 K
200 K
250 K
300 K
PL intensity (arb. units)
Photon energy (eV)

Fig. 3

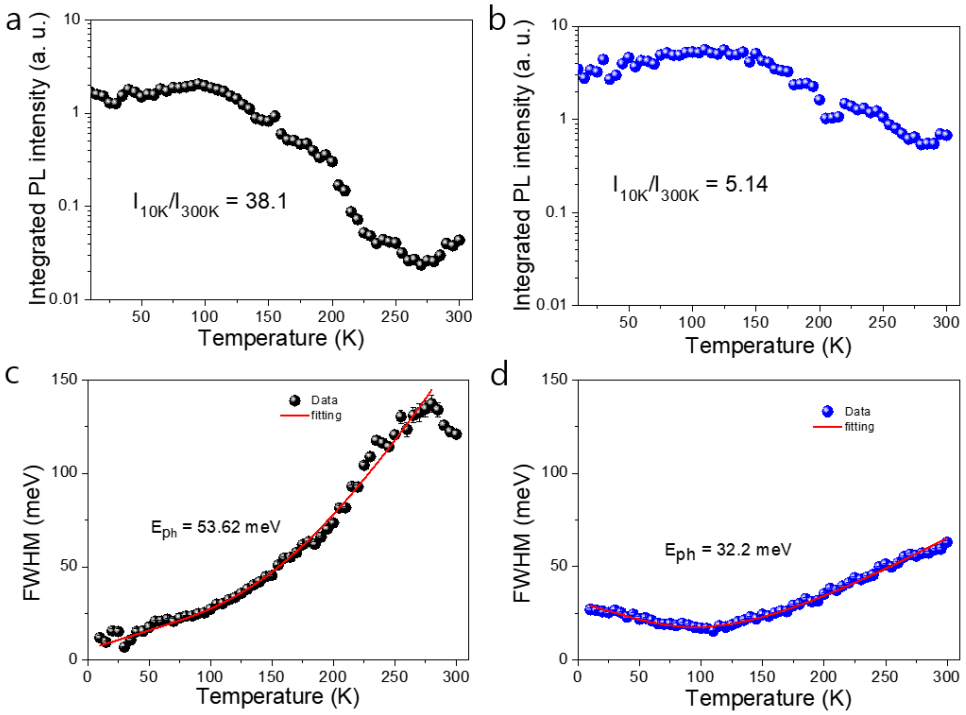
a
b
c
d
Integrated PL intensity (a. u.)
Temperature (K)
I10K/I300K = 38.1
I10K/I300K = 5.14
FWHM (meV)
Data
fitting
Eph = 53.62 meV
Eph = 32.2 meV

Fig. 4

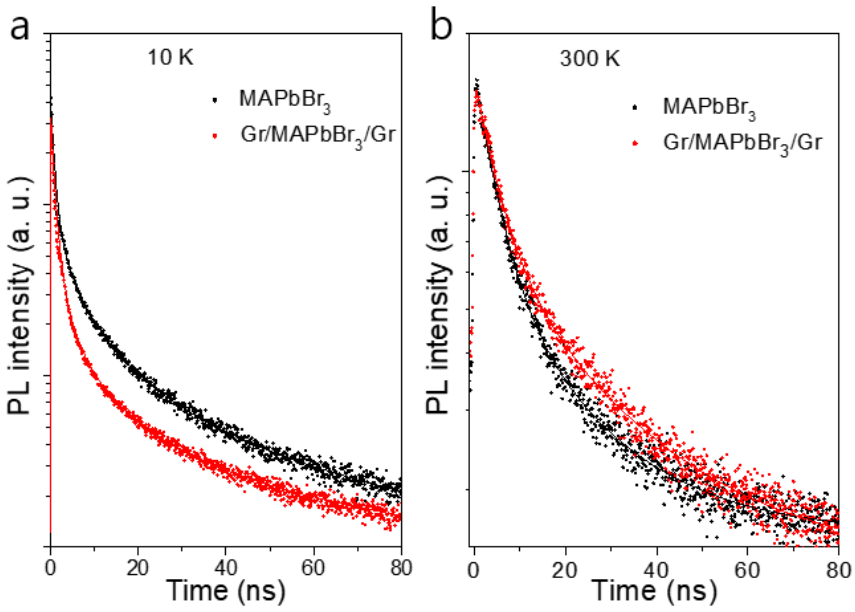
a
10 K
MAPbBr3
Gr/MAPbBr3/Gr
PL intensity (a. u.)
0
20
40
60
80
Time (ns)
b
300 K
MAPbBr3
Gr/MAPbBr3/Gr
PL intensity (a. u.)
0
20
40
60
80
Time (ns)

Fig. 5.

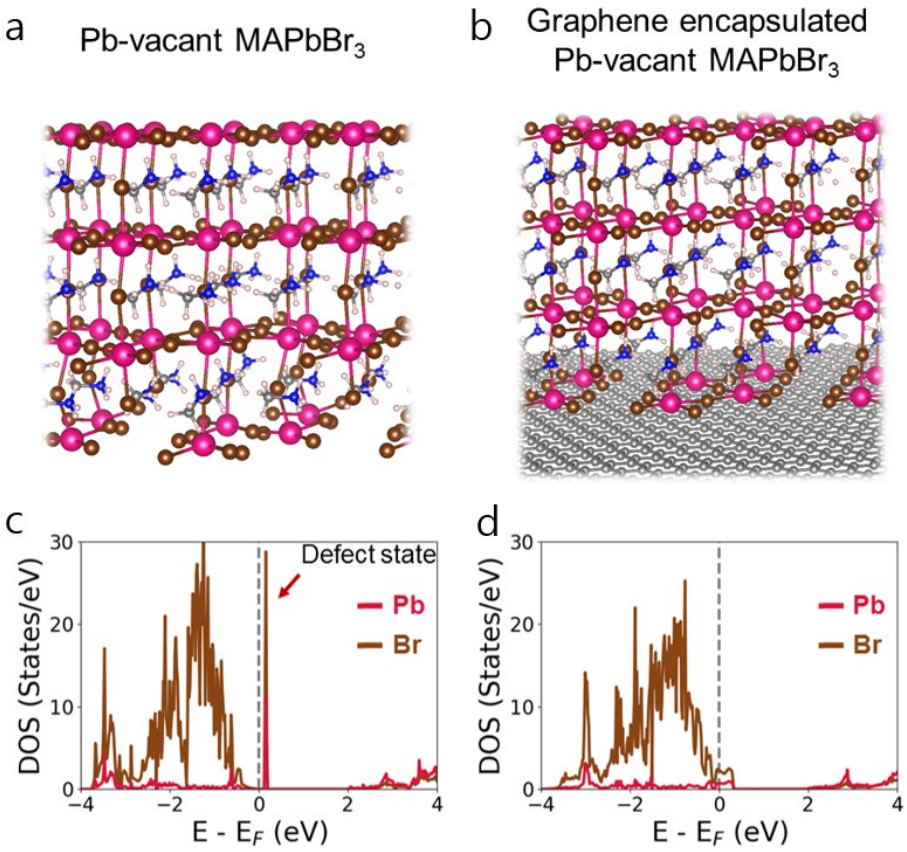
a
Pb-vacant MAPbBr3
b
Graphene encapsulated
Pb-vacant MAPbBr3
c
Defect state
Pb
Br
DOS (States/eV)
30
20
10
0
−4
−2
0
2
4
E - EF (eV)
d
Pb
Br
DOS (States/eV)
30
20
10
0
−4
−2
0
2
4
E - EF (eV)

Fig. 6